Journal of Materials Chemistry C

Role of excess tellurium on the electrical and thermal properties in Te-doped paracostibite

Journal:	*Journal of Materials Chemistry C*
Manuscript ID	TC-ART-09-2019-004840.R1
Article Type:	Paper
Date Submitted by the Author:	16-Dec-2019
Complete List of Authors:	Guélou, Gabin; University of Reading, Department of Chemistry Failamani, Fainan; National Institute for Materials Science, Thermal Energy Materials Group Sauerschnig, Philipp; National Institute for Materials Science Waybright, Jace; National Institute for Materials Science SUZUTA, Keiko; Tsukuba Daigaku Mori, Takao; National Institute for Materials Science,

Role of excess tellurium on the electrical and thermal properties in Te-doped paracostibite

G. Guélou[1], F. Failamani[1], P. Sauerschnig[1], J. Waybright[1], K. Suzuta[1] and T. Mori[1,2]

[1] National Institute for Materials Science (NIMS), International Center for Materials Nanoarchitectonics (WPI-MANA) and Center for Functional Sensor & Actuator (CFSN), Namiki 1-1, Tsukuba 305-0044, Japan

[2] University of Tsukuba, Graduate School of Pure and Applied Sciences, 1-1-1 Tennoudai, Tsukuba 305-8671, Japan

MORI.Takao@nims.go.jp

The effect of excess Te in the preparation of synthetic mineral paracostibite, CoSbS, was investigated in an attempt to produce a nano-micro-porous architecture. While the latter was found to have no significant impact, we demonstrate that such strategy is a successful approach to enhance both electrical and thermal property via the formation of a more Te-rich paracostibite phase compared with conventional substitution. Tuning of the electrical properties led to a large power factor of 2150 μW m^{-1} K^{-2} at 765 K while the lattice thermal conductivity was reduced by ca. 45%, mainly due to an increased electron-phonon scattering. Ultimately, a maximum ZT of 0.45 was achieved, representing a 100% improvement over conventional Te-doped paracostibite.

Introduction

The need for sustainable energy sources that do not rely on the combustion of fossil fuel has never been more crucial. In this context, efforts are being made toward improvement and large-scale application of environmentally friendly renewable energy sources as well as implementing energy-harvesting devices in existing industrial processes.[1] The waste-heat generated by these processes can be converted into electrical power using thermoelectric (TE) devices operating in the appropriate temperature range; additionally, such devices can be used to harvest natural energy such as heat from sunlight or from the human body.[2–5] Thus, TE materials have the potential to access a broad range of applications ranging from everyday gadgets such as body-heat powered watches to versatile solid-state heat pumps. In order to extricate the TE technology from the current niche applications, low-cost materials with good performances and low-toxicity are required.[6] The performance of a TE material can be related to its electrical and thermal transport properties via the dimensionless figure of merit $ZT = S^2\sigma T/\kappa$, where S, σ and κ are the Seebeck coefficient, electrical and thermal conductivities respectively. One way of improving the TE properties of a material beyond charge carrier optimisation or band structure/correlation related effects, is to look for novel effects and/or extrinsic effects such as grain size, morphology and boundary engineering.[7–9]

Controlled porosity has been shown to lead to dramatic improvement of the TE response by means of selective phonon scattering.[10,11] Indeed, targeting the heat-carrying phonons over the charge carriers is made possible by the difference in mean free path, much shorter in the case of the latter and less sensitive

to scattering arising from interactions with nano-micrometer scale pores. The difficulty also lies in the distribution of size and repartition of pores across the sample that impacts the phonons over a specific range of wavelengths.[10,12] In this context, a balance must be achieved between the complexity of the pores array, the reduction in thermal conductivity and the often inevitable loss in electrical conductivity.[13–15] For instance, while nanomesh structures may give rise to dramatic reduction in thermal conductivity,[13] they also constitute a major obstacle for large scale application. A particularly successful approach recently led to a 100% improvement in ZT for a rare-earth free skutterudite by means of nano-micro pore formation through second phase evaporation.[16] In this work, we investigate the effect of excess tellurium and second phase evaporation in a different family of materials with a higher proportion of earth-abundant sulphur, the intermetallic paracostibite.

Paracostibite, CoSbS (space group Pbca) was first identified by Harris et al.[17] in 1970 as a naturally occurring mineral from the Red Lake mine in Ontario, Canada, along with a related phase, costibite, CoSbS (space group $Pnm2_1$), extracted from Broken Hill, Australia.[18] The latter has only been synthesised for a substantial amount of Se substitution on the sulphur site, $CoSbS_{1-x}Se_x$ ($x \geq 0.75$), with rather poor TE performance.[19] Paracostibite has attracted a growing attention in the past few years following the work of Carlini *et al*.[20] and Parker *et al*.[21] whose investigation emphasised on the potential of paracostibite from the band structure stand point, in particular owing to the high band degeneracy near the band edges. High throughput DFT point defect calculations and the subsequent experimental studies revealed that Te substitution on the antimony site was an excellent way to achieve extremely high electrical performances with a power factor of 2700 $\mu W\ m^{-1}\ K^{-2}$ over the temperature range $543 \leq T / K \leq 730$ K.[22,23] To the best of our knowledge, this remains the highest power factor achieved in an *n*-type sulphide. This rather recent addition to the sulphur-based family of TE materials can provide a much needed *n*-type counterpart to the performing *p*-type Cu-based sulphides such as tetrahedrites,[24,25] bornites,[26,27] thiospinels,[28] germanite[29,30] or colusites.[31–34] While current *n*-type sulphides have made huge progress in the last few years, they do remain somewhat behind their *p*-type counterparts in term of TE performance. Some promising examples include TiS_2 derivatives,[35–40] $Cu_4Sn_7S_{16}$,[41] or chalcopyrites.[42–44] Unfortunately, the overall TE response of Te-doped paracostibite remains hindered by its high thermal conductivity despite the convincing reductions achieved in κ through selenium substitution.[19] The combination of good electrical and poor thermal transport properties makes Te-doped paracostibite an ideal candidate to investigate the effect of second phase evaporation.

Experimental

In order to confirm the optimum Te doping, previously established to be around 4% Te_{Sb},[23] a first series with stoichiometry $CoSb_{1-x}Te_xS$ ($x = 0, 0.01, 0.03, 0.04, 0.05$) was prepared by solid-state reaction in a carbon-coated sealed evacuated quartz tube. Two series were investigated to account for the possible effects of slight off-stoichiometry on the Co and S sites, $Co_{1+x}Sb_{0.96}Te_{0.04}S$ ($x = -0.02, -0.01, 0, 0.01, 0.02, 0.03, 0.04$) and $CoSb_{0.96}Te_{0.04}S_{1+z}$ ($z = -0.05, -0.02, 0, 0.02, 0.05$). Finally, we produced a series containing extra Te in order to form a second phase to be expelled during SPS and annealing. The initial compositions was $CoSb_{0.96}Te_{0.04+y}S$ ($y = 0.07, 0.14, 0.21, 0.28$); for clarity these samples will be labelled as $CoSb_{0.96}Te_{0.04}S[Te]_y$.

For all series, the synthesis and spark plasma sintering conditions were the same. Pure elements, Co (Sigma Aldrich, powder, 99.95 %), Sb (5N Plus, shots, 99.999%), Te (5N Plus, shots, 99.999%) and S (Sigma Aldrich, flakes, 99.99%) were weighted, thoroughly ground in an agate mortar and cold-pressed prior to being evacuated down to *ca*. 10^{-3} mbar. The ampoules were then subjected to a first heat treatment in a muffle furnace at 573 K for 24h then 923 K for 48h with heating and cooling rates of 1 K min^{-1}. The process was repeated on the obtained powders including intermediate grinding and cold-pressing for a second firing at 923 K for 48h. The collected samples were once again thoroughly ground in an agate mortar and sieved down to 100 µm prior to SPS treatment (SPS-1080 System, SPS SYNTEX Inc.). The latter was conducted in a 10 mm diameter graphite die under a uniaxial pressure of 50 MPa in argon at 923 K for 15 min with heating and cooling rates of 1.5 K s^{-1}. The pressure was kept on until the temperature decreased below 373 K. For the series containing an excess of Te, the consolidated samples were polished and subjected to another 24h of annealing at 923 K to ensure the second phase was fully evaporated. The final pellets (*ca*. 4-5 mm thickness and 10 mm diameter) were then cut laterally to obtain two disks, with one of them cut for electrical transport property measurements and the other one polished to an even thickness for thermal diffusivity measurement. Powder X-ray diffraction analysis (XRD) was carried out at room temperature on a Rigaku SmartLab 3 diffractometer over the 2θ range of 10–90° in steps of 0.02° using Cu-K_α radiation. Rietveld analysis was carried out using the GSAS software package.[45,46] Scanning electron micrographs were acquired on a Hitachi FE-SEM SU8000 scanning electron microscope (SEM) at 10 kV, and elemental analysis were carried out on samples polished by standard metallographic procedures using electron probe microanalysis (JEOL IXA-8500F) with wavelength-dispersive X-ray spectroscopy (WDX) operated at 15 kV. The temperature dependences of the electrical resistivity, ρ, and the Seebeck coefficient, S, were measured simultaneously on a *ca*. 2 x 2 x 8 mm bar over the temperature range 323 ≤ T/K ≤ 773 using a ULVAC ZEM-2 under a partial pressure of He. The thermal diffusivity, δ, was measured on 10 mm disks of thickness 1.5-2 mm using a Netzch LFA467 Hyperflash under nitrogen flow. At each temperature point, five measurements were carried out and the averaged results were used to determine the thermal conductivity, $\kappa = \delta d C_p$. The specific heat, C_p, for CoSbS, $CoSb_{0.96}Te_{0.04}S$ and $CoSb_{0.96}Te_{0.04}S[Te]_{0.28}$ samples were determined from DSC analysis using a NETZSCH STA 449 F3 Jupiter; thermo-gravimetric analysis (TGA) was conducted simultaneously. The determined specific heats above room temperature were all within *ca*. 10 % of the Dulong-Petit value. Finally, the lattice contribution to the thermal conductivity was determined by subtracting the estimated electronic component from the measured total thermal conductivity, κ. The estimated experimental error is 6% for the Seebeck coefficient, 8% for the electrical resistivity, 11% for the thermal conductivity, and 16% for the figure of merit, ZT.[47]

Results and discussion

An initial series of Te-substituted paracostibite, $CoSb_{1-x}Te_xS$ (x = 0, 0.01, 0.03, 0.04, 0.05), confirmed that a 4% Te substitution for Sb was the optimum doping to maximise ZT, consistent with previous observations, Fig. S1-S3.[23] From this, $CoSb_{0.96}Te_{0.04}S$ will be used as a reference to investigate the effect of Te excess on the TE properties and will be referred to as the pristine phase. X-ray diffraction analysis and Rietveld refinement confirmed the formation of single-phase $CoSb_{0.96}Te_{0.04}S$, (Fig. 1a) that crystallises in a Pbca orthorhombic structure with unit cell parameters a = 5.8425(1) Å, b = 5.9563(1) Å and c =

11.6671(2) Å. The rather simple structure, isostructural to the marcasite FeS_2, consists in corner-sharing distorted $CoSb_3S_3$ octahedra sharing one additional edge.[48] The resulting stiff bonding in a fairly small unit cell (24 atoms / unit cell) involving light anions is believed to be responsible for the high average sound velocity and high thermal conductivity of the material.[21] Samples prepared with excess Te were determined to be a mixture of paracostibite and Sb_2Te_3, Fig. 1(b), which melts at around 893 K[49] and is consequently partially melted out during SPS and fully evaporated during subsequent annealing under vacuum.

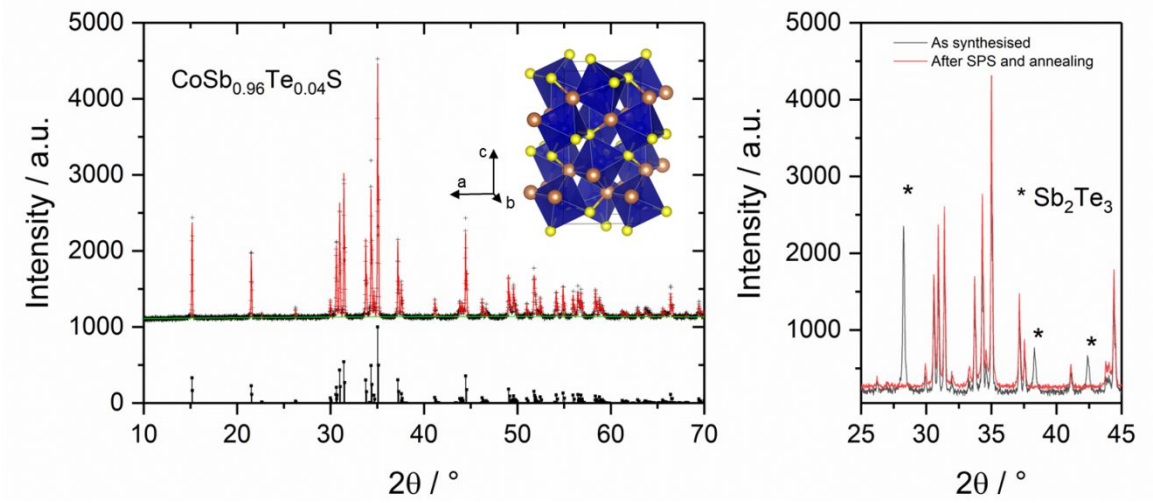

Fig. 1 (a) Acquired X-ray diffraction patterns (black crosses) and refined model (red line) for $CoSb_{0.96}Te_{0.04}S$. Peaks with calculated relative intensities are shown; the crystal structure (Pbca) of paracostibite is given as an inset. **(b)** The superimposed XRD patterns of $CoSb_{0.96}Te_{0.04}S[Te]_{0.28}$ before and after SPS and annealing.

SEM imaging confirmed the formation of pores of various sizes and shape, Fig. 2, and the marked differences caused by the addition of excess Te in the process. In the pristine sample, Fig. 2(a,b), the distribution of particle size is very narrow with homogeneous shapes. The sample appears fully dense and devoid of pores while samples prepared with excess Te, Fig. 2(c,d), show a very different morphology. Different sizes and types of pores are clearly identifiable with submicron scale cavities sprouting on the surface of the larger grains and a significant concentration of micrometer-scale pores at the grain boundaries. It is also worth noting that the particle size distribution appears to be less homogeneous, suggesting that the excess Te may also encourage grain growth, Fig. S4.

The electrical properties of paracostibite upon Te substitution and $CoSb_{0.96}Te_{0.04}S$ exposed to Te excess are given in Fig. S2 and Fig. 3 respectively. All samples have negative Seebeck coefficient, confirming the majority charge carriers to be electrons. Upon 4% Te substitution, paracostibite moves from a semiconducting to a much more degenerate behaviour with an electrical resistivity decreasing from 2.3 mΩ m and 0.084 mΩ m to 0.065 mΩ m and 0.041 mΩ m at 325 K and 750 K respectively (Fig. S2), confirming previous observations.[22,23] This decrease is accompanied by a large reduction in the magnitude of the Seebeck coefficient, consistent with an increase in the charge carrier concentration. As

a result, the power factor for Te-doped paracostibite reaches 1200 μW m^{-1} K^{-2}, a nearly 55% increase over that of undoped paracostibite. The addition of excess Te in the synthesis process has a dramatic impact on the electrical properties of Te-doped paracostibite, Fig. 3. The electrical resistivity and magnitude of the Seebeck coefficient steadily decrease upon the addition of excess Te, demonstrating that the intentional formation of a second phase (Sb_2Te_3) and its later removal has an impact on the composition of the paracostibite phase that differs from simple Te/Sb substitution. The addition of excess Te is illustrated by the 80 % rise in the power factor from 1200 μW m^{-1} K^{-2} to 2150 μW m^{-1} K^{-2} at 765 K for $CoSb_{0.96}Te_{0.04}S[Te]_{0.28}$, despite the small increase in the sample porosity. The mechanisms behind the enhancement of power factor beyond Te/Sb substitution, are yet to be fully understood and we do not expect the formation of pores to be responsible for tuning the electrical properties. Additionally, we do not expect our observations to be caused by liquid-flow assisted SPS, despite the similarities in the process[50,51] because the temperatures involved are much higher and the annealing time allows for grain-growth and composition homogenisation. Such a process previously led to high performance in $(Bi,Sb)_2Te_3$.[52] We also excluded a possible scenario where variations in Co and S stoichiometry would be responsible for the observed variations by exploring the electrical properties of two series $Co_{1+x}Sb_{0.96}Te_{0.04}S$ (x = -0.02, -0.01, 0, 0.01, 0.02, 0.03, 0.04) and $CoSb_{0.96}Te_{0.04}S_{1+z}$ (z = -0.05, -0.02, 0, 0.02, 0.05), Fig. S5. No substantial changes were observed. Additionally, the effect of extended exposure to high temperature was also discarded as a potential factor with no variations in the electrical properties observed after 1 week at 923 K, Fig. S5. However, we can consider two possible scenarios where: (1) the excess Te shifts the overall sample composition towards different phase field which favours an equilibrium with Te-richer paracostibite, thus increasing the solubility limit beyond the reported values,[23,53] and (2) the difference in the synthesis temperature between this work and the literature (see supplementary information) changes the solubility, which is commonly observed. The first scenario was observed in other TE systems, e.g. skutterudites,[54,55] and has been proven to be a useful strategy to boost the materials performance. Additionally, the presence of a large amount of Te and the formation a Sb_2Te_3 secondary phase could shift the chemical potential towards a more Te-rich paracostibite with fewer compensating electron-killing defects than simple substitution.[56]

The increase of the Te solubility is further confirmed by the significant increase of the unit cell volume, as well as the WDX measurement, Fig. S6-S7, Table S1. The measured Sb/Te ratio exhibit rather large variation between different grains in the sample (Table S1). Nevertheless, the averaged Te content (x in $CoSb_{1-x}Te_xS$) showed an increase up to 0.074 in the sample with 28% extra Te with the maximum measured Te content up to 0.10, close to the estimated value from lattice parameter assuming the validity of Vegard's law. The overall composition shift is further confirmed by the existence of a small amount of CoS secondary phase (Fig. S8), in addition to the liquid phase. It seems that equilibrium with CoS promotes higher Te solubility, as observed in the previous report.[53] A comprehensive phase equilibrium study of the quaternary Co-Sb-S-Te system is required to shed more details on this matter.

A closer inspection of the electrical transport properties was carried out using a relationship proposed by Min and Rowe[57] where the Seebeck coefficient can be related to the electrical conductivity via a simple equation:

$$S = \frac{k_B}{e}(b - \ln \sigma) \qquad \text{(eq. 1)}$$

The parameter *b* contains a $T^{3/2}(m^*/m_0)^{3/2}\mu$ term, which allow us to qualitatively estimate and compare the weighed mobility $(m^*/m_0)^{3/2}\mu$. This approach has been shown to be quite useful to analyse the electrical transport properties of various type of materials.[58–61]

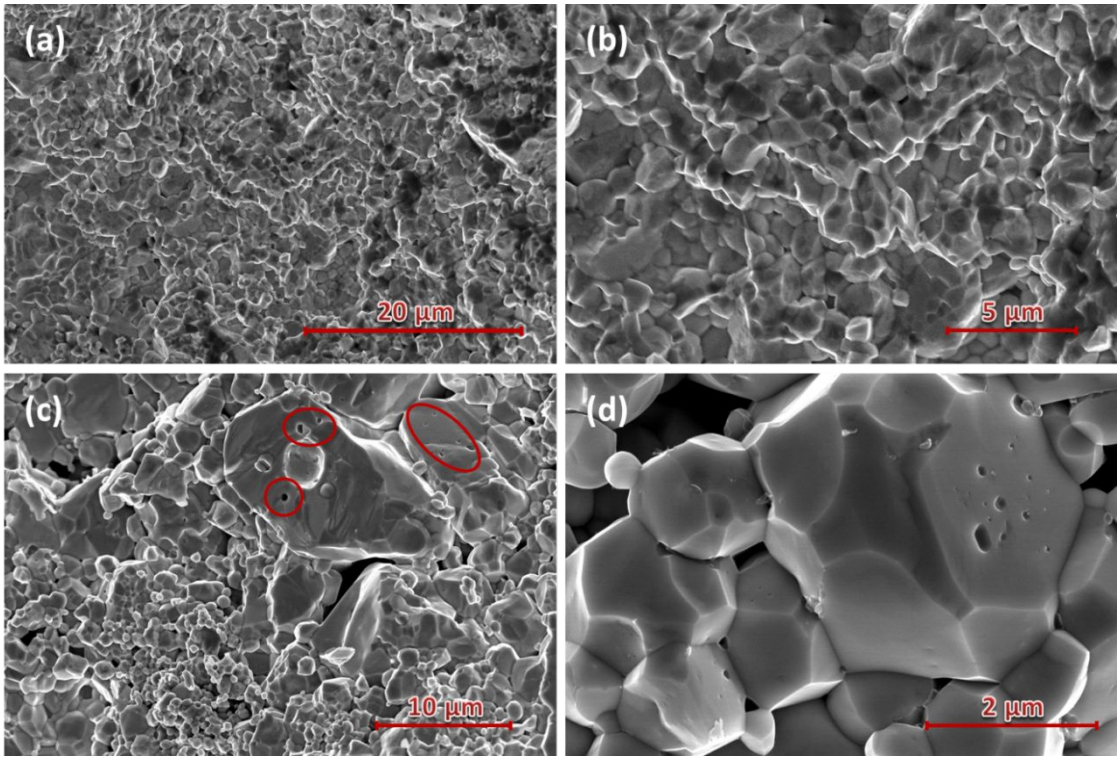

Fig. 2 Scanning electron micrographs of a fractured surface after SPS and annealing of **(a,b)** $CoSb_{0.96}Te_{0.04}S$ and **(c,d)** $CoSb_{0.96}Te_{0.04}S[Te]_{0.28}$ samples. Nanometer scale pores can be clearly observed on the surface of the larger particles.

A Seebeck vs ln σ plot with a constant slope of $\frac{k_B}{e}$, depicted in Fig. 4 reveals that data from pristine Te substituted $CoSb_{1-x}Te_xS$ ($0.01 \leq x \leq 0.05$) samples lie around the same *b* value, while $CoSb_{0.96}Te_{0.04}$ samples with excess Te are located further away (i.e. correspond to higher *b* values) from the pristine Te substituted paracostibite. Interestingly, the parameter *b* for samples with excess Te increases concomitantly with increasing excess Te amount, indicating an increase in weighed mobility with increasing excess Te. The increased weighed mobility could be related to the alignment of the carrier pockets, possibly due to unit volume expansion.[23] We have also previously observed enhancement of the power factor via enhancement of the effective mass, i.e. Seebeck coefficient, through magnetic interactions[61,62] or spin fluctuations[63], so these possibilities should be considered in future investigations coupled with the magnetic properties investigations.

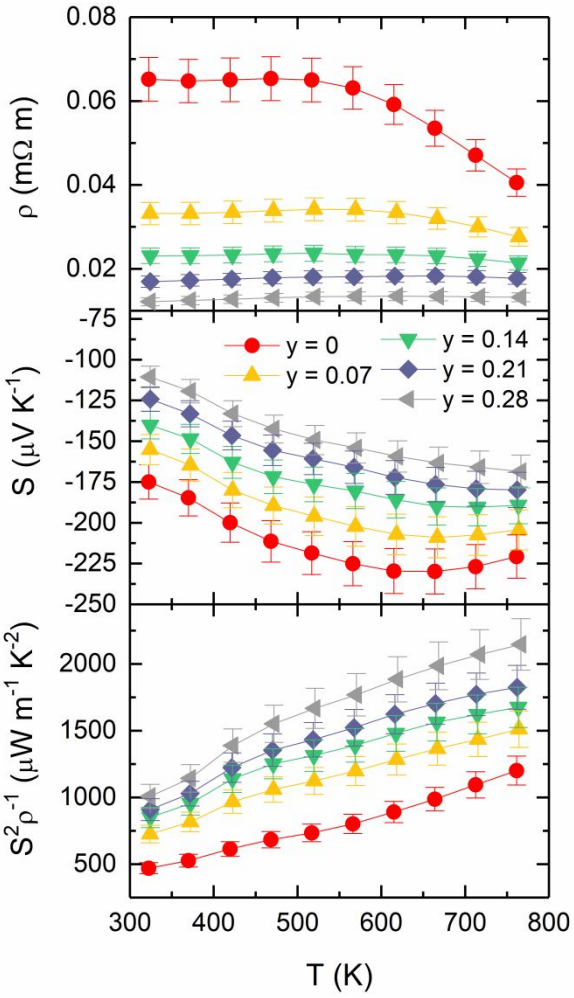

Fig. 3 Temperature dependence of the electrical resistivity, Seebeck coefficient and power factor for pristine $CoSb_{0.96}Te_{0.04}S$ and $CoSb_{0.96}Te_{0.04}S[Te]_y$.

Comparing our data with the previously published results, particularly the Te doped paracostibite, it is interesting to see that some of the previously reported data at room temperature scatter around the same line as the pristine Te-doped samples at 100°C. Exceptions to this are the 2% Te doped[23] and 7% Te doped[53] that are located above and below our pristine Te doped samples, respectively. This observation agrees well with the measured mobility and effective mass where Chmielowski *et al*. reported a significantly enhanced electron mobility in 2% Te doped sample (almost 300%), while You *et al*. reported approximately 60% reduction in 7% Te doped samples, compared to the undoped paracostibite. A plausible explanation to this discrepancy could be related to the difference in the synthesis method, which could strongly affect the defect formations, and consequently the electrical transport properties.

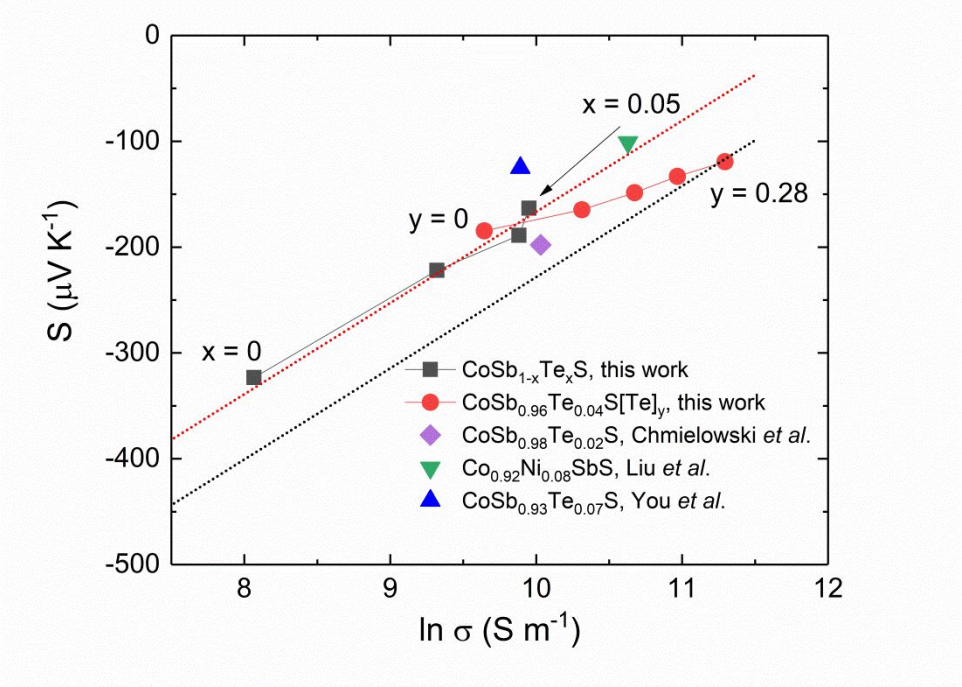

Fig. 4 Seebeck coefficient as a function of ln σ for $CoSb_{1-x}Te_xS$ ($0.01 \leq x \leq 0.05$) and $CoSb_{0.96}Te_{0.04}S[Te]_y$ compared with samples from Chmielowski *et al*.[23], Liu *et al*.[64] and You *et al*.[53] The dotted lines are based on eq. 1 with a *b* value of 11.82 and 12.68 for the red and black dotted lines respectively.[57]

Upon 4% Te/Sb substitution, we observe a small decrease in the total thermal conductivity at room temperature, Fig. S2. Addition of excess Te, Fig. 5, reduces the thermal conductivity further at room temperature, however it becomes less significant at higher temperature. When the addition of excess Te reaches y = 0.28, a more significant reduction over the whole temperature range is obtained. Since the electrical resistivity is significantly improved by the addition of excess Te, the electronic contribution to the thermal conductivity becomes more significant in this sample. In order to quantify the lattice contribution to the overall thermal conductivity, we subtracted the electronic contribution to the thermal conductivity, which was calculated assuming the validity of Wiedemann-Franz law:

$$\kappa_{el} = L\sigma T \qquad \text{(eq. 2)}$$

where L is the Lorenz number, estimated from the Seebeck coefficient using the simplified relationship, *L* = 1.5 + exp(-|S|/116), described by Kim *et al*.[65] Fig. 5 clearly shows a significant reduction of the lattice thermal conductivity by the addition of excess Te, approximately by 45 % for $CoSb_{0.96}Te_{0.04}S[Te]_{0.28}$. Since this sample also contains a larger amount of Te, one would expect more contribution from point defect scattering, particularly near room temperature. In order to quantify this contribution, we use the model from Abeles and Slack:[66,67]

$$\frac{\tan^{-1} a}{a} = \frac{\kappa_L^{doped}}{\kappa_L^{pure}} \text{ and } a^2 = \frac{\pi^2 \theta_D \Omega \kappa_L^{pure} \Gamma}{h v_s} \qquad \text{(eq. 3)}$$

where

$$\Gamma = \frac{1}{3}\left(\frac{\overline{m}}{M_{ave}}\right)^2 x(1-x)\left(\left(\frac{\Delta m}{\overline{m}}\right)^2 + \varepsilon\left(\frac{\Delta r}{\overline{r}}\right)^2\right) \quad \text{(eq. 4)}$$

and

$$\overline{m} = xM_{Te+}(1-x)M_{Sb} \quad \text{(eq. 5)}$$

and

$$\overline{r} = xr_{Te+}(1-x)r_{Sb} \quad \text{(eq. 6)}$$

where Γ is the disorder scattering parameter and ε is an adjustable parameter that depends on the Grüneisen parameter, γ. Using the adjusted ε value of 38.61 from the same system,[53] the calculated lattice thermal conductivities from point defect scattering at 323 K are listed in table 1. For samples without excess Te, the calculated lattice thermal conductivity agrees with the measured value within the measurement uncertainty. For samples with excess Te, the measured values are significantly lower than the calculated lattice thermal conductivity.

Table 1 Disorder scattering parameter, measured (Wiedemann-Franz law) and calculated (Point-defect scattering) lattice contribution to the thermal conductivity and their percentage difference for $CoSb_{0.96}Te_{0.04}S[Te]_y$ compared with pristine CoSbS and $CoSb_{0.96}Te_{0.04}S$.

Sample	x in $CoSb_{1-x}Te_xS$	Γ_{calc} ($\times 10^{-3}$)	$\kappa_L^{Measured}$ (W m^{-1} K^{-1})	κ_L^{Calc} (W m^{-1} K^{-1})	Difference (%)
CoSbS	0	-	9.99	-	-
$CoSb_{0.96}Te_{0.04}S$	0.04	0.4063	9.30	9.891	6.2
$CoSb_{0.96}Te_{0.04}S[Te]_{0.07}$	0.059*	0.5839	8.03	9.850	20.4
$CoSb_{0.96}Te_{0.04}S[Te]_{0.14}$	0.079*	0.7671	7.27	9.809	29.7
$CoSb_{0.96}Te_{0.04}S[Te]_{0.21}$	0.087*	0.8368	6.93	9.793	34.2
$CoSb_{0.96}Te_{0.04}S[Te]_{0.28}$	0.125*	1.1388	4.94	9.726	65.3

* Estimated from unit cell volume

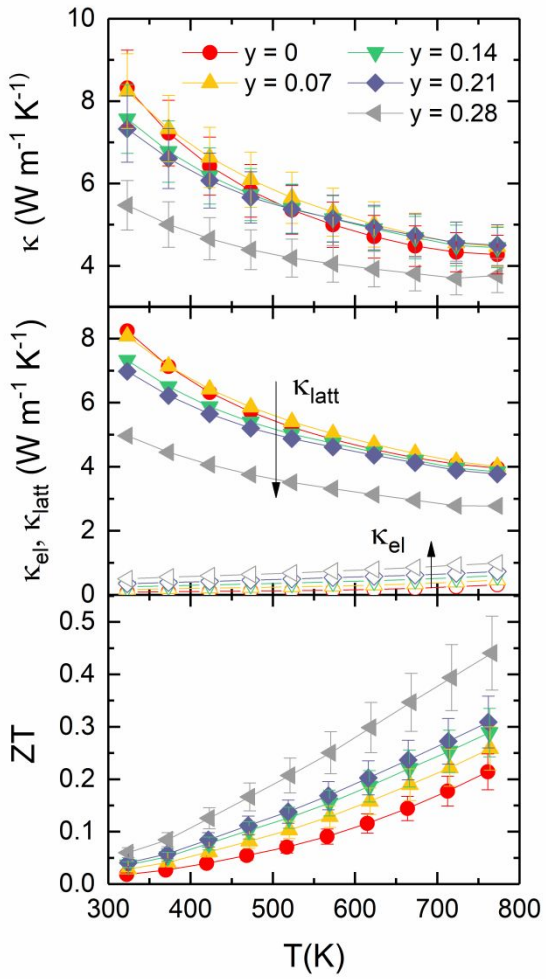

Fig. 5 Temperature dependence of the total thermal conductivity, the electronic and lattice contribution to the thermal conductivity and figure of merit ZT for pristine $CoSb_{0.96}Te_{0.04}S$, and $CoSb_{0.96}Te_{0.04}S[Te]_y$.

In order to further elucidate the mechanism of the reduction of the lattice thermal conductivity, additional scattering mechanisms were introduced into the Debye-Callaway model,[68]

$$\kappa_l = \frac{k_B}{2\pi^2 v_a}\left(\frac{k_B T}{\hbar}\right)^3 \int_0^{\theta_D/T} \tau_C \frac{x^4 e^x}{(e^x-1)^2} dx \qquad \text{(eq. 7)}$$

where k_B is the Boltzmann constant, v_a is the average speed of sound, $\hbar$ is the reduced Planck`s constant, x is the reduced frequency ($\hbar\omega/k_BT$), θ_D is the Debye temperature, and τ_C is the total relaxation time calculated based on Matthiesen's rule considering grain boundary scattering, Umklapp scattering and electron phonon scattering in addition to the point defect scattering :

$$\frac{1}{\tau_C} = \sum \frac{1}{\tau_i} = \frac{1}{\tau_{PD}} + \frac{1}{\tau_U} + \frac{1}{\tau_{GB}} + \frac{1}{\tau_{PE}} \qquad \text{(eq. 8)}$$

The relaxation times for each scattering processes are defined as:

$$\frac{1}{\tau_{PD}} = A\omega^4 \ ; \ A = \frac{V_a}{4\pi {v_a}^3}\Gamma \qquad \text{(eq. 9)}$$

where V_a is the average atomic unit cell volume;

$$\frac{1}{\tau_{GB}} = \frac{v_a}{d} \qquad \text{(eq. 10)}$$

where *d* is the average grain size;

$$\frac{1}{\tau_U} = B\omega^2 T \exp\left(\frac{-\theta_D}{3T}\right) \qquad \text{(eq. 11)}$$

$$\frac{1}{\tau_{PE}} = C\omega \mathrm{T} \qquad \text{(eq. 12)}$$

Following the analysis made by Liu *et al.*,[64] assuming that the Debye temperature, speed of sound and the relaxation time of Umklapp scattering are independent of doping, one could extract the τ_U directly from the undoped sample. It is interesting to note that the extracted τ_U and τ_{PE} relaxation constant (*A* and *C*, respectively) from the undoped sample are in the same range as in the work of Liu *et al*.. Analysis was performed for data below 600 K in order to minimise the bipolar effect. Moreover, the τ_U for the doped samples were allowed to vary ±10% from the undoped sample.

As expected from the small difference between the mass and size of Sb and Te, the point defect scattering does not contribute significantly to the reduction of the lattice thermal conductivity of paracostibite (Table 2). As with Ni-doped paracostibite,[64] the electron-phonon scattering seems to dominate the scattering process in the Te doped paracostibite, where the relaxation constant *C* increase by one order of magnitude from 2.7×10^{-3} to 28.8×10^{-3}. The increase of the electron phonon relaxation constant *C* is much smaller compared to that of Ni-doped paracostibite (over 5 orders of magnitude), indicating weaker electron-phonon interaction in Te doped paracostibite. A weaker electron-phonon interaction is illustrated by a smaller deformation potential, and thus, higher carrier mobility, which is consistent with the higher weighted mobility in our case (Fig. 4).

Table 2 Fitting parameters based on Debye Callaway model.

Sample	$A_{calculated}$	B	C
CoSbS	0	4.11×10^{-18}	2.89×10^{-3}
$CoSb_{0.96}Te_{0.04}S$	8.21×10^{-45}	3.96×10^{-18}	4.50×10^{-3}
$CoSb_{0.96}Te_{0.04}S[Te]_{0.07}$	1.18×10^{-44}	3.70×10^{-18}	1.15×10^{-2}
$CoSb_{0.96}Te_{0.04}S[Te]_{0.14}$	1.55×10^{-44}	3.70×10^{-18}	1.51×10^{-2}
$CoSb_{0.96}Te_{0.04}S[Te]_{0.21}$	1.69×10^{-44}	3.70×10^{-18}	1.68×10^{-2}
$CoSb_{0.96}Te_{0.04}S[Te]_{0.28}$	2.31×10^{-44}	4.52×10^{-18}	2.88×10^{-2}

Based on the analysis above, it can be concluded that the pore formation does not significantly affect the lattice thermal conductivity as expected. The level of porosity obtained in this study seems to be

insufficient to have a significant impact, which could be different for each studied system. Indeed, the measured density only decreases from 96% to 93% of the crystallographic value for $CoSb_{0.96}Te_{0.04}S$ and $CoSb_{0.96}Te_{0.04}S[Te]_{0.28}$ respectively. The relatively high temperature and long sintering duration are likely to be responsible for this. A longer sintering, at temperatures above the melting point of the precipitated secondary phase, means less amount of secondary phase left in the sintered pellets, and thus, a lower amount of pores produced after annealing.

Following the simultaneous improvement of the electrical and thermal properties of Te-doped paracostibite, the calculated ZT is largely improved over the whole investigated temperature range with a maximum of 0.45(7) reached at 773 K. This corresponds to a 100% improvement over simple Te-doped paracostibite, $CoSb_{0.96}Te_{0.04}S$, and a 300% improvement over pristine CoSbS. This performance is amongst the best reported in doped paracostibite with higher ZT obtained only for co-doped samples such as $CoSb_{0.96}Te_{0.04}S_{0.75}Se_{0.25}$, that still holds the record with ZT = 0.62 at 730 K.[19] Estimation of minimum lattice thermal conductivity based on the random walk between Einstein oscillator[69] gives a value of approximately 1 W m^{-1} K^{-1}, which is three times lower than the lowest lattice thermal conductivity in obtained in this study (2.73 W m^{-1} K^{-1} at 766 K) and approximately half of the lowest lattice thermal conductivity (≈ 2 W m^{-1} K^{-1}) in the work of Chmielowski *et al*..[19] This suggests that there is still significant room for improvement in thermoelectric paracostibite, particularly for the reduction in the lattice thermal conductivity.

Conclusions

Overall, while the initial objective of improving the TE response of Te-doped paracostibite was met, the nano-micrometer scale pores did not play the predominant role expected in the 100% improvement in ZT at 773 K. Nonetheless, we showed that the reduction in the lattice contribution to the thermal conductivity could not simply be attributed to point defect scattering. The concentration of pores, and therefore their contribution to the reduction in the thermal conductivity, may have been significantly reduced by the rather harsh sintering conditions necessary to obtain robust samples. Overall, we demonstrated that using excess tellurium during the synthesis was a successful strategy to optimise both electrical and thermal properties simultaneously. We showed that the excess Te led to a significant increase in the unit cell volume, likely to be a consequence of the formation of a more Te-rich paracostibite, beyond the solubility limit of conventional substitution. This unit cell expansion can be linked to the enhanced electrical performance via an increase in weighted mobility that could be resulting from carrier pocket alignment or possible magnetic effects, which will be investigated in detail in the future. Finally, it is worth noting that, beyond the good overall thermoelectric performance illustrated by the figure of merit, carrier-doped paracostibite also exhibits a high power factor, particularly for a sulphur-rich intermetallic. This is strongly desirable as the overall output power density of the TE device depends on it.

Conflicts of interest

There are no conflicts to declare.

Acknowledgements

Support from CREST JPMJCR15Q6, JPMJCR19Q4 and JSPS KAKENHI JP17H02749, JP16H06441, JP19H00833 is acknowledged.

Notes and references

[1] D. M. Rowe, *Renew. Ener.* **1999**, *16*, 1251.

[2] G. Min, D. M. Rowe, In *CRC Handbook of Thermoelectrics*; Rowe, D. M., Ed.; CRC Press, 1995.

[3] L. E. Bell, *Science (80-.).* **2008**, *321*, 1457.

[4] J. He, T. M. Tritt, *Science (80-.).* **2017**, *357*, eaak9997.

[5] I. Petsagkourakis, K. Tybrandt, X. Crispin, I. Ohkubo, N. Satoh, T. Mori, *Sci. Technol. Adv. Mater.* **2018**, *19*, 836.

[6] C. B. Vining, *Nat. Mater.* **2009**, *8*, 83.

[7] J. Mao, Z. Liu, J. Zhou, H. Zhu, Q. Zhang, G. Chen, Z. Ren, *Adv. Phys.* **2018**, *67*, 69.

[8] T. Mori, *Small* **2017**, *13*, 1.

[9] T. Mori and T. Hara, *Scripta Mater.* **2016**, 111, 44.

[10] J. Tang, H.-T. Wang, D. H. Lee, M. Fardy, Z. Huo, T. P. Russell, P. Yang, *Nano Lett.* **2010**, *10*, 4279.

[11] B. Xu, T. Feng, Z. Li, S. T. Pantelides, Y. Wu, *Nano Lett.* **2018**, *18*, 4034.

[12] J. Lee, J. Lim, P. Yang, *Nano Lett.* **2015**, *15*, 3273.

[13] J.-K. Yu, S. Mitrovic, D. Tham, J. Varghese, J. R. Heath, *Nat. Nanotechnol.* **2010**, *5*, 718.

[14] P. E. Hopkins, C. M. Reinke, M. F. Su, R. H. Olsson, E. A. Shaner, Z. C. Leseman, J. R. Serrano, L. M. Phinney, I. El-Kady, *Nano Lett.* **2011**, *11*, 107.

[15] N. Zen, T. A. Puurtinen, T. J. Isotalo, S. Chaudhuri, I. J. Maasilta, *Nat. Commun.* **2014**, *5*, 3435.

[16] A. U. Khan, K. Kobayashi, D.-M. Tang, Y. Yamauchi, K. Hasegawa, M. Mitome, Y. Xue, B. Jiang, K. Tsuchiya, D. Golberg, Y. Bando, T. Mori, *Nano Energy* **2017**, *31*, 152.

[17] D. C. Harris, J. M. Stewart, L. J. Cabri, *Can. Mineral.* **1970**, *10*, 232.

[18] L. J. Cabri, Harris, J. M. Stewart, *Am. Mineral.* **1970**, *55*, 10.

[19] R. Chmielowski, S. Bhattacharya, S. Jacob, D. Péré, A. Jacob, K. Moriya, B. Delatouche, P. Roussel, G. Madsen, G. Dennler, *Sci. Rep.* **2017**, *7*, 1.

[20] R. Carlini, C. Artini, G. Borzone, R. Masini, G. Zanicchi, G. A. Costa, *J. Therm. Anal. Calorim.* **2011**, *103*, 23.

[21] D. Parker, A. F. May, H. Wang, M. A. McGuire, B. C. Sales, D. J. Singh, *Phys. Rev. B - Condens. Matter Mater. Phys.* **2013**, *88*, 159902.

[22] S. Bhattacharya, R. Chmielowski, G. Dennler, G. K. H. Madsen, *J. Mater. Chem. A* **2016**, *4*, 11086.

[23] R. Chmielowski, S. Bhattacharya, W. Xie, D. Péré, S. Jacob, R. Stern, K. Moriya, A. Weidenkaff, G. K. H. H. Madsen, G. Dennler, *J. Mater. Chem. C* **2016**, *4*, 3094.

[24] K. Suekuni, K. Tsuruta, T. Ariga, M. Koyano, *Appl. Phys. Express* **2012**, *5*, 2.

[25] R. Chetty, A. Bali, R. C. Mallik, *J. Mater. Chem. C* **2015**, *3*, 12364.

[26] G. Guélou, A. V. Powell, P. Vaqueiro, *J. Mater. Chem. C* **2015**, *3*, 10624.

[27] P. Qiu, T. Zhang, Y. Qiu, X. Shi, L. Chen, *Energy Environ. Sci.* **2014**, *7*, 4000.

[28] A. U. Khan, R. A. R. A. Orabi, A. Pakdel, J. B. Vaney, B. Fontaine, R. Gautier, J. F. Halet, S. Mitani, and T. Mori, *Chem. Mater.* **2017**, 29, 2988.

[29] V. Pavan Kumar, L. Paradis-Fortin, P. Lemoine, V. Caignaert, B. Raveau, B. Malaman, G. Le Caër, S. Cordier, E. Guilmeau, *Inorg. Chem.* **2017**, *56*, 13376.

[30] V. Pavan Kumar, L. Paradis-Fortin, P. Lemoine, G. Le Caer, B. Malaman, P. Boullay, B. Raveau, G. Guélou, E. Guilmeau, *ACS Appl. Energy Mater.* **2019**, *online*.

[31] C. Bourgès, Y. Bouyrie, A. R. Supka, R. Al Rahal Al Orabi, P. Lemoine, O. I. Lebedev, M. Ohta, K. Suekuni, V. Nassif, V. Hardy, R. Daou, Y. Miyazaki, M. Fornari, E. Guilmeau, *J. Am. Chem. Soc.* **2018**, *140*, 2186.

[32] V. Pavan Kumar, A. R. Supka, P. Lemoine, O. I. Lebedev, B. Raveau, K. Suekuni, V. Nassif, R. Al Rahal Al Orabi, M. Fornari, E. Guilmeau, *Adv. Energy Mater.* **2018**, *9*, 1803249.

[33] K. Suekuni, T. Takabatake, *APL Mater.* **2016**, *4*.

[34] V. Pavan Kumar, G. Guélou, P. Lemoine, B. Raveau, A. Supka, R. Al Rahal Al Orabi, M. Fornari, K. Suekuni, E. Guilmeau, *Angew. Chemie Int. Ed.* **2019**, *0*.

[35] Y. Wang, L. Pan, C. Li, R. Tian, R. Huang, X. Hu, C. Chen, N. Bao, K. Koumoto, C. Lu, *J. Mater. Chem. C* **2018**, *6*, 9345.

[36] C. Bourgès, T. Barbier, G. Guélou, P. Vaqueiro, A. V. Powell, O. I. Lebedev, N. Barrier, Y. Kinemuchi, E. Guilmeau, *J. Eur. Ceram. Soc.* **2016**, *36*.

[37] E. Guilmeau, A. Maignan, C. Wan, K. Koumoto, *Phys. Chem. Chem. Phys.* **2015**, *17*, 24541.

[38] F. Gascoin, N. Raghavendra, E. Guilmeau, Y. Bréard, *J. Alloys Compd.* **2012**, *521*, 121.

[39] M. Beaumale, T. Barbier, Y. Bréard, G. Guelou, A. V. Powell, P. Vaqueiro, E. Guilmeau, *Acta Mater.* **2014**, *78*, 86.

[40] G. Guélou, P. Vaqueiro, J. Prado-Gonjal, T. Barbier, S. Hébert, E. Guilmeau, W. Kockelmann, A. V. Powell, *J. Mater. Chem. C* **2016**, *4*.

[41] C. Bourgès, P. Lemoine, O. I. Lebedev, R. Daou, V. Hardy, B. Malaman, E. Guilmeau, *Acta Mater.* **2015**, *97*, 180.

[42] R. Lefèvre, D. Berthebaud, M. Y. Mychinko, O. I. Lebedev, T. Mori, F. Gascoin, A. Maignan, *RSC Adv.* **2016**, *6*, 55117.

[43] N. Tsujii and T. Mori, *Applied Physics Express* **2013**, 6, 043001.

[44] R. Ang, A. U. Khan, N. Tsujii, K. Takai, R. Nakamura, and T. Mori, Angew. Chem. Int. Ed. **2015**, 54, 12909.

[45] A. C. Larson, R. B. Von Dreele, *Los Alamos Natl. Lab. Rep. LAUR 86-748* **1994**.

[46] B. Toby, *J. Appl. Crystallogr.* **2001**, *34*, 210.

[47] E. Alleno, D. Bérardan, C. Byl, C. Candolfi, R. Daou, R. Decourt, E. Guilmeau, S. Hébert, J. Hejtmanek, B. Lenoir, P. Masschelein, V. Ohorodnichuk, M. Pollet, S. Populoh, D. Ravot, O. Rouleau, M. Soulier, *Rev. Sci. Instrum.* **2015**, *86*, 11301.

[48] J. F. Rowland, E. J. Gabe, S. R. Hall, *Can. Mineral.* **1975**, *13*, 188.

[49] J. Rumble, *CRC Handbook of Chemistry and Physics*; 99th ed.; CRC Press: Boca Raton, 2018.

[50] H. Mun, K. H. Lee, S. J. Yoo, H. S. Kim, J. Jeong, S. H. Oh, G. J. Snyder, Y. H. Lee, Y. M. Kim, S. W. Kim, *Acta Mater.* **2018**, *159*, 266.

[51] S. Il Kim, K. H. Lee, H. A. Mun, H. S. Kim, S. W. Hwang, J. W. Roh, D. J. Yang, W. H. Shin, X. S. Li, Y. H. Lee, G. J. Snyder, S. W. Kim, *Science (80-.).* **2015**, *348*, 109.

[52] Y. Pan, Y. Qiu, I. Witting, L. Zhang, C. Fu, J. W. Li, Y. Huang, F. H. Sun, J. He, G. J. Snyder, C. Felser and J. F. Li, *Energy Environ. Sci.* **2019**,12, 624.

[53] Y. You, X. Su, W. Liu, Y. Yan, J. Fu, X. Cheng, C. Zhang, X. Tang, *J. Solid State Chem.* **2018**, *262*, 1.

[54] Y. Tang, S. Chen, G. J. Snyder, *J. Mater.* **2015**, *1*, 75.

[55] A. Grytsiv, P. Rogl, H. Michor, E. Bauer, G. Giester, *J. Electron. Mater.* **2013**, *42*, 2940.

[56] A. Zunger, *Appl. Phys. Lett.* **2003**, *83*, 57.

[57] D. M. Rowe, G. Min, *J. Mater. Sci. Lett.* **1995**, *14*, 617.

[58] E. S. Toberer, M. Christensen, B. B. Iversen, G. J. Snyder, *Phys. Rev. B* **2008**, *77*, 75203.

[59] E. S. Toberer, A. F. May, B. C. Melot, E. Flage-Larsen, G. J. Snyder, *Dalt. Trans.* **2010**, *39*, 1046.

[60] B. Jalan, S. Stemmer, *Appl. Phys. Lett.* **2010**, *97*, 42106.

[61] F. Ahmed, N. Tsujii, T. Mori, *J. Mater. Chem. A* **2017**, *5*, 7545.

[62] N. Tsujii, A. Nishide, J. Hayakawa, T. Mori, *Sci. Adv.* **2019**, *5*, eaat5935.

[63] J.-B. Vaney, S. Aminorroaya Yamini, H. Takaki, K. Kobayashi, N. Kobayashi, T. Mori, *Mater. Today*

Phys. **2019**, *9*, 100090.

[64] Z. Liu, H. Geng, J. Shuai, Z. Wang, J. Mao, D. Wang, Q. Jie, W. Cai, J. Sui, Z. Ren, *J. Mater. Chem. C* **2015**, *3*, 10442.

[65] H.-S. Kim, Z. M. Gibbs, Y. Tang, H. Wang, G. J. Snyder, *APL Mater.* **2015**, *3*, 41506.

[66] B. Abeles, *Phys. Rev.* **1963**, *131*, 1906.

[67] G. S. Nolas, H. J. Goldsmid, In *Thermal Conductivity: Theory, Properties, and Applications*; Tritt, T. M., Ed.; Springer US: Boston, MA, 2004; pp. 105–121.

[68] J. Callaway, *Phys. Rev.* **1959**, *113*, 1046.

[69] D. C. Cahill, S. K. Watson, R. O. Pohl, *Phys. Rev. B* **1992**, *46*, 6131.

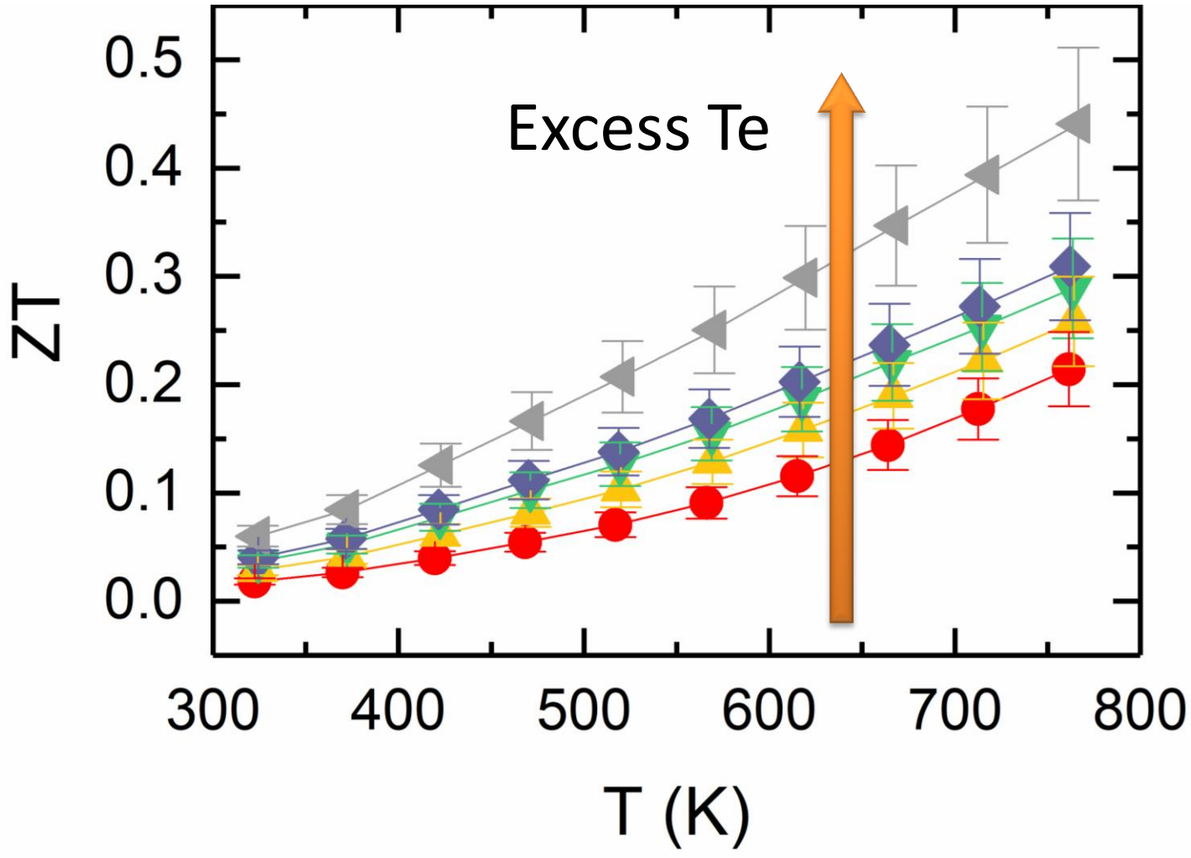
Excess Te
ZT
0.0
0.1
0.2
0.3
0.4
0.5
300
400
500
600
700
800
T (K)